Original Article

DOI: 10.5582/ddt.2026.01050

Unveiling the allosteric inhibition mechanism of SARS-CoV-2 main protease and discovery of a novel allosteric inhibitor

Quanling Zhang[1], Tingting Wen[1], Mengsi Li[1], Xiaowen Tang[1,2,*]

[1] Department of Medicinal Chemistry, School of Pharmacy, Qingdao University, Qingdao, China;
[2] Shandong Key Laboratory of Pathogenesis and Prevention of Brain Diseases, Qingdao University, Qingdao, China.

SUMMARY: The severe acute respiratory syndrome coronavirus 2 (SARS-CoV-2) main protease (Mpro) is a crucial therapeutic target for anti-coronavirus disease 2019 (COVID-19) drug development, as it is essential for viral replication. However, mutations within the active site have compromised the efficacy of current competitive inhibitors, prompting the exploration of alternative inhibition strategies. In this study, we systematically investigated the allosteric inhibition mechanism of SARS-CoV-2 Mpro by pelitinib and leveraged this insight for new inhibitor discovery. Through extensive molecular dynamics simulations, we showed that pelitinib exerts allosteric inhibition *via* the L141-S144-C145-H41 interaction network: it restricts the flexibility of L141 through CH-π interactions, transmits this effect to C145 *via* S144, stabilizes the hydrogen bond between C145 and H41, and thereby reduces the flexibility of the S3 helix (residues 40–60). This series of conformational changes induces the contraction of the Mpro catalytic pocket from ~1200 Å³ to ~800 Å³, impairs substrate binding, and ultimately appears to impair Mpro activity. Based on this mechanism, we performed structure-based virtual screening and identified a novel compound (Cpd-1). Biological evaluations showed that Cpd-1 exhibits superior Mpro inhibitory activity compared to pelitinib, with negligible off-target binding to human EGFR and Myt1 kinase, low cytotoxicity (cell viability > 60% at 200 μM), and predicted inhibitory activity against clinically relevant Mpro-resistant mutants based on computational analysis. Our findings provide mechanistic insights into a key allosteric mechanism for Mpro inhibition but also provide a promising chemical scaffold for further development as an Mpro-targeting inhibitor.

Keywords: SARS-CoV-2 main protease, allosteric inhibition mechanism, molecular dynamics simulations

1. Introduction

The coronavirus disease 2019 (COVID-19) pandemic is caused by a novel human coronavirus, namely severe acute respiratory syndrome coronavirus 2 (SARS-CoV-2), which has resulted in an unprecedented number of infections and deaths globally (*1-3*). In response to this pandemic, extensive efforts have been devoted to the development of Mpro inhibitor. To date, multiple small-molecule drugs (*e.g.*, paxlovid (*4*), simnotrelvir (*5*), leritrelvir (*6*), and ensitrelvir (*7*)) and vaccines (*e.g.*, BNT162b2 (*8*), ZyCov-D (*9*), Ad5-nCov (*10*), and BBIBP-CorV (*11*)) have been approved for clinical use, contributing to the prevention and treatment of COVID-19. However, although vaccines can rapidly establish herd immunity, the inherent nature of SARS-CoV-2 as an RNA virus renders it highly prone to mutations. Such mutations significantly compromise the protective efficacy of vaccines (*12,13*), highlighting an urgent need for the development of effective small-molecule Mpro inhibitors.

SARS-CoV-2 is an enveloped, positive-sense single-stranded RNA virus classified within the genus *Betacoronavirus* of the family Coronaviridae (*14*). Its genome is approximately 30,000 nucleotides in length, sharing 79% and 50% sequence homology with severe acute respiratory syndrome coronavirus (SARS-CoV) and Middle East respiratory syndrome coronavirus (MERS-CoV), respectively (*15*). Similar to other viruses, the replication, expression, and assembly of the viral genetic material constitute the core stages of its infection cycle (*16*). Upon entry into host cells, SARS-CoV-2 releases its genomic RNA, which is then translated into polyproteins pp1a and pp1ab. These polyproteins are subsequently cleaved by papain-like protease (PLpro) and main protease (Mpro) to generate a series of non-structural proteins (Nsps), which further facilitate viral replication through assembly processes (*16,17*). Notably, Mpro is responsible for cleaving at 11 sites within the polyproteins, making it a key enzyme essential for viral replication (*16*). It is worth emphasizing that PLpro shares high structural similarity

with human deubiquitinating enzymes, raising the risk of off-target effects for its inhibitors (*12*). Conversely, Mpro has no homologous protein in human hosts (*18*), endowing it with great potential for highly selective inhibition (*19*). Thus, Mpro is recognized as an ideal therapeutic target for Mpro inhibitor development.

Current research on Mpro inhibitors primarily focuses on targeting its active site, aiming to block viral replication through direct competitive inhibition of enzymatic activity (*20*). For instance, nirmatrelvir, which exhibits potent inhibitory activity against SARS-CoV-2 Mpro, has been developed for COVID-19 treatment and received FDA approval on May 25, 2023 under the trade name Paxlovid (*4*). Other clinically approved Mpro-targeting inhibitors include simnotrelvir (*5*), leritrelvir (*6*), ensitrelvir (*7*), and atilotrelvir (*21*). However, under the selective pressure exerted by competitive inhibitors, SARS-CoV-2 Mpro has acquired adaptive mutations, leading to the emergence of various drug-resistant strains (*22*). For example, mutations at residues F140, M49, and E166 in SARS-CoV-2 Mpro can significantly reduce the inhibitory activity of competitive inhibitors against SARS-CoV-2. Specifically, the E166V mutation increases the half-maximal inhibitory concentration (IC_{50}) of nirmatrelvir and ensitrelvir by 300-fold and 78-fold (*23*), respectively. The occurrence of such drug resistance necessitates the exploration of alternative inhibitory strategies in the field of Mpro inhibitor development. Allosteric inhibitors, which bind to remote allosteric sites on enzymes to induce conformational changes and modulate the function of active sites, offer a promising solution to overcome the aforementioned challenges (*24-26*). Günther *et al.* and Samrat *et al.* have successfully identified a series of allosteric inhibitors of SARS-CoV-2 Mpro (*e.g.*, pelitinib, RS102895, ifenprodil (*27*), and JMX series compounds including JMX0286, JMX0301, and JMX0941 (*28*)) through allosteric modulation strategies targeting non-active sites of Mpro. Among these inhibitors, pelitinib exhibits the most prominent inhibitory activity against SARS-CoV-2 with a half-maximal effective concentration (EC_{50}) of 1.25 μM. (*27*). However, as a compound originally developed for antitumor activity, pelitinib can significantly inhibit human membrane-associated tyrosine/threonine protein kinase 1 (Myt1 kinase) and epidermal growth factor receptor (EGFR), leading to severe off-target effects (*29,30*). Additionally, the molecular mechanism underlying the allosteric inhibition of SARS-CoV-2 Mpro remains unclear, which has hindered the further development of its allosteric inhibitors.

In this study, we focused on the allosteric inhibition of SARS-CoV-2 Mpro by pelitinib. By using integrated molecular dynamics (MD) simulations, virtual screening, and bioassay strategies, we systematically investigated the allosteric inhibition mechanism of SARS-CoV-2 Mpro and further identified novel allosteric inhibitors based on this mechanism. Our results demonstrated that pelitinib regulates the conformation of the S3 helix through the L141-S144-C145-H41 interaction network, which induces the contraction of the catalytic pocket and blocks substrate binding, thereby inhibiting Mpro activity. Based on this mechanism, we successfully screened a novel compound (designated as Cpd-1). Biological activity assays showed that Cpd-1 exhibited significantly improved Mpro inhibitory activity (IC_{50} = 74.3 μM) compared with pelitinib (IC_{50} = 148.3 μM). Moreover, Cpd-1 displayed excellent target selectivity and low cytotoxicity. Furthermore, Cpd-1 retained potent inhibitory activity against multiple drug-resistant mutants of SARS-CoV-2 Mpro, demonstrating its potential to overcome drug resistance. Collectively, this study proposes a molecular mechanism for allosteric inhibition of Mpro and identifies a candidate compound with favorable activity, selectivity, and anti-resistance properties, providing a new strategy and theoretical basis for the development of Mpro-targeting inhibitors.

2. Materials and Methods

2.1. Molecular dynamics simulations

The initial structures of the SARS-CoV-2 Mpro, Myt1 kinase, and EGFR were retrieved from the RCSB Protein Data Bank (*31*) (detailed information is listed in Table S1, *https://www.ddtjournal.com/action/getSupplementalData.php?ID=315*). All receptor-ligand complexes were constructed based on co-crystal structures or through molecular docking. All Molecular Dynamics (MD) Simulations were performed with AMBER24 (*32,33*). The Amber ff19SB force field (*34*) was employed for the protein, and the TIP3P model (*35*) was used for the solvent water molecules. The force field parameters of ligands were generated from the general AMBER force field (GAFF), and the partial atomic charge was defined by the restrained electrostatic potential (RESP) (*36*) charge based on HF/6-31G* calculation with the Gaussian09 package.

The initial coordinates and topology files were generated by the tleap module with neutralization and solvation. The subsequent classical MD simulations were carried out by using the periodic boundary condition with the cubic model. After a series of energy minimization, programmed heating (0 to 310 K, NVT, 100 ps), density equilibrium (310 K, 1.0 atm, NPT, 100 ps), and pre-equilibrium (310 K, 1.0 atm, NPT, 2 ns), a final long-term scale MD simulation (200 or 500 ns as listed in Table S1, *https://www.ddtjournal.com/action/getSupplementalData.php?ID=315*) with a 2 fs time step were performed under the NVT ensemble to generate trajectories. During the MD simulation, the high-frequency stretching vibration of all hydrogen-

containing bonds was constrained by using the SHAKE algorithm (*37*), and a 12 Å cutoff was applied to van der Waals (LJ-12 potential) and electrostatic interactions (PME strategy). Finally, cpptraj was used for trajectories analysis and PyMOL was used for visualization.

Adaptively Biased Molecular Dynamics (ABMD) (*38*) simulations in AMBER24 were employed for the two systems (Mpro-nsp4/5, and Mpro-nsp4/5-Pelitinib) to map out the free energy profiles of natural substrate (nsp4/5) binding in different states. The distance between the sulfur atom in C145 and the carbon atom of the carbonyl group in Gln of nsp4/5 was defined as the collective variable (CV). The Gaussian bias with spatial directionality was used to drive the substrate from an initial position away from the catalytic site (CV = 27.0 Å) toward the active center (CV = 3.0 Å). The hills and widths were set to 0.1 kcal/mol and 0.5 Å, respectively. The Gaussian bias potential was added to the potential energy surface at every 5 ps. The time step of ABMD was set to 2 fs. In total, the ABMD simulation time were set to 100 ns for the two systems.

Pocket volumes of Mpro in various systems along the MD simulations were calculated using POVME3.0 (*39*). C145 was chosen to define the pocket, and the parameter GridSpacing was set to 1.0 Å. Additionally, the MM-PBSA (*40*) method was employed to calculate the binding free energy of the ligand to the receptor. The trajectory from the stable MD simulation stage was used to calculate the pocket volume and binding free energy. More than 2,000 frames were extracted from the stable MD trajectory at regular intervals for the calculations in each system.

2.2. Virtual screening

The screening library was constructed using the Drug-like and Lead-like subsets from the ZINC20 database. Subsequently, through molecular fingerprint similarity analysis based on Tanimoto coefficient in SwissSimilarity (*41*) platform, molecules with structural similarity to Pelitinib greater than 80% were retained to ensure that the candidate compounds maintain the known affinity to the target. It should be noted that the Tanimoto coefficient based molecular fingerprint similarity used here reflects similarities in local chemical environments rather than global 2D scaffold identity. Thus, the screened compounds could exhibit distinct scaffold from Pelitinib but retain the key pharmacophore features essential for allosteric inhibition. The three-dimensional (3D) pharmacophore model was constructed by using Molecular Operating Environment (MOE) (*42*) software, based on the Pelitinib-Mpro complex. Particular attention was paid to the amino acid L141, which is crucial to the allosteric inhibition mechanism. The 3D pharmacophore model was then employed to perform virtual screening against the screening library. Ultimately, 228 candidate compounds were identified and utilized for the subsequent docking-based virtual screening.

By selectively retaining the Apo-Mpro dimer (PDB ID: 6XHU) and integrating the Holo-Mpro monomer (pelitinib-bound complex, PDB ID: 7AXM), a pelitinib-bound SARS-CoV-2 Mpro dimer complex was obtained and utilized as the receptor model for molecular docking. The molecular docking was performed by using AutoDock Vina (*43*). The protonation states of titratable residues in receptor and ionizable groups in compounds were determined under conditions of pH 7.0 ± 0.2, mimicking the actual physiological environment. The ligand (pelitinib) in receptor model was used to define the center of the docking grid, with the grid dimensions set to 25 × 25 × 25 $Å^3$. The flexible docking strategy was ultimately executed based on the induced-fit theory, and the binding mode with the optimal docking score, along with the corresponding docking results, was recorded.

The pharmacokinetic properties and druggability (adsorption, distribution, metabolism, excretion, and toxicity, ADMET) of the screened compounds were predicted by using SwissADME (*44*) (*https://www.swissadme.ch/*), ADMETlab3.0 (*45*) (*https://admetlab3.scbdd.com/*), and ProTox-3.0 (*46*) (*https://tox-new.charite.de/*) platform.

The selected hit compound Cpd-1 (ZINC11613113, SMILES: C1=COC(=C1)CN2C(=O)C=C(C2=O)NC3=CC=C(C=C3)S(=O)(=O)N) was purchased from MCE (MedChemExpress, Monmouth Junction, NJ, USA, Cat. # HY-L0096V, Lot # 676256) as part of the Vitas-M Screening Compounds Library.

2.3. Enzymatic assays

The inhibitory activity of the identified compounds on Mpro was assessed using the 2019-nCoV Mpro/3CLpro Inhibitor Screening Kit (Beyotime, Shanghai, China, P0312S). The 2019-nCov Mpro/3CLpro enzyme, at a volume of 1 μL, was exposed to Dabcyl-KTSAVLQSGFRKME-Edansin a 96-well plate at 4ºC. Subsequently, negative control (DMSO) and positive control (Ebselen) were added to the plate, along with samples at concentrations ranging from 6.25 μM to 800 μM (6.25 μM, 12.5 μM, 25 μM, 50 μM, 100 μM, 200 μM, 400 μM, 800 μM). Finally, substrate with a volume of 2 μL was added, and the plate was incubated for 10 minutes at 37ºC. The fluorescence of the final system was measured at excitation and emission wavelengths of 340 nm and 490 nm, respectively, using a multifunctional fluorescence microplate reader (Thermo Fisher Scientific, Waltham, MA, USA).

2.4. Cytotoxicity measurement

Cell viability and cytotoxicity assays were conducted

in BEAS-2B cells (Beyotime, Shanghai, China; human bronchial epithelial cells) using the Cell Counting Kit-8 (CCK-8, MeilunBio, Dalian, Liaoning, China), following the manufacturer protocol. Initially, cells were seeded at a density of 6 × 10^3 cells per well in a volume of 100 µL. After incubation overnight at 37°C in a humidified atmosphere with 5% CO_2. The cells were treated with protease inhibitors at different concentrations. After 16 hours of treatment, 10 µL of the CCK-8 solution was added to each well of the plate using a repeating pipette, and the plate was incubated for an additional 1 hours. Absorbance was measured at a wavelength of 450 nm using a BioTek Synergy HT microplate reader (BioTek Instruments, Winooski, VT, USA).

2.5. Statistical analysis

All statistical analyses were performed using GraphPad Prism 9.0 (GraphPad Software, San Diego, CA, USA). Data were extracted from the molecular dynamics simulation trajectory and further presented as mean ± standard deviation (SD). Comparisons among multiple groups were conducted using one-way analysis of variance (ANOVA), followed by post hoc multiple comparisons with letter annotations to indicate between-group differences: groups labeled with the same letter are not statistically different, while groups labeled with different letters (*e.g.*, a *vs*. b) differ significantly, with a significance threshold set at $p < 0.0001$.

3. Results

3.1. Allosteric inhibitors induce contraction of the Mpro catalytic pocket

To investigate the effects of allosteric inhibitors (*e.g.*, pelitinib) on the structure of Mpro, MD simulations were performed on six systems, including Mpro monomer, Mpro dimer, and ligand-Mpro complexes. The root-mean-square deviation (RMSD) values of all six systems remained stable throughout the 500 ns simulation, confirming the reliability of the results (Figure S1, *https://www.ddtjournal.com/action/getSupplementalData.php?ID=315*). Subsequent calculations of the catalytic pocket volume in each system revealed that, as shown in Figure 1A, the catalytic pocket volume of Mpro was approximately 1,200 Å³ in systems where Mpro activity was not inhibited (dimer and negative control group: PD168568-Mpro complex (*27*)). In contrast, the pocket volume was reduced to approximately 800 Å³ in systems where Mpro activity was inhibited (monomer, Pelitinib-Mpro, RS102895-Mpro, and Ifenprodil-Mpro complexes (*27*)). These results suggest that the volume of the Mpro catalytic pocket is a key indicator of its activity state. As illustrated in Figure 1B, the active state (~1,200 Å³) significantly enhances substrate binding efficiency by expanding the substrate-binding cavity, whereas the inactive state (~800 Å³) impairs substrate binding through shrinking the substrate-binding pocket, ultimately leading to the loss of enzymatic activity.

To further explore the intrinsic mechanism by which pocket volume affects enzymatic activity, ABMD simulations were employed to calculate the free energy changes during the binding of the natural substrate (nsp4/5) to Mpro in both active and inactive states. As shown in Figure 2, in the active state, the substrate could move from the external region into the catalytic site (with a distance of ~5 Å between the

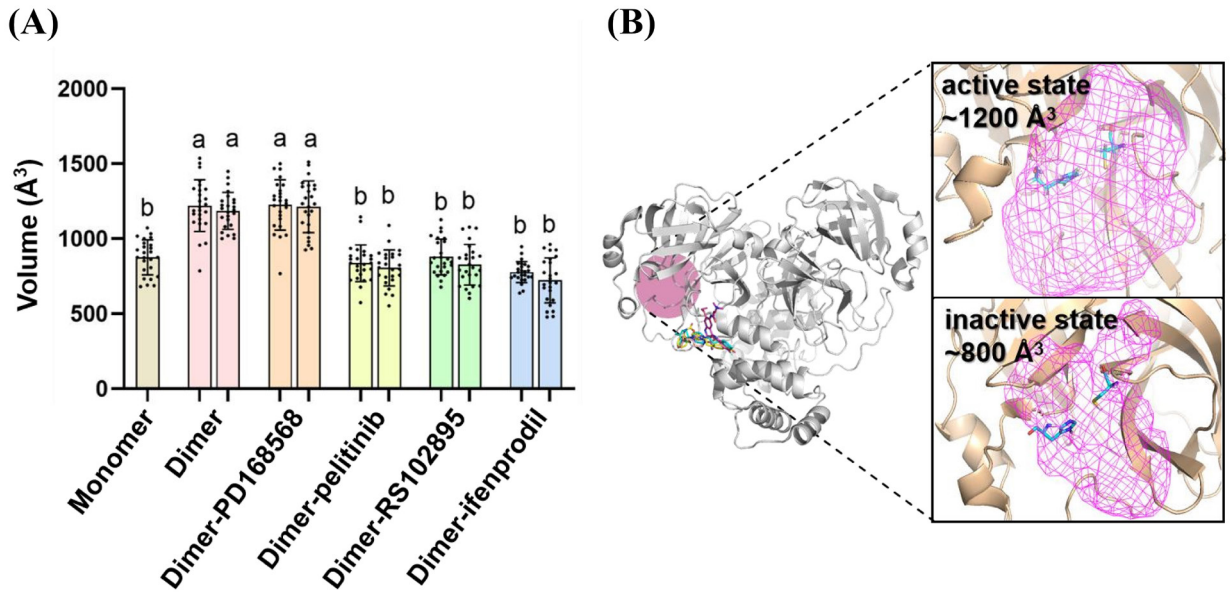

Figure 1. (A) Catalytic pocket volume of Mpro in the six systems through MD simulation, groups labeled with different letters differed significantly (a *vs.* b, $p < 0.0001$). **(B)** Relationship model between the Mpro catalytic pocket volume and its catalytic activity. The pocket is depicted by pink mesh.

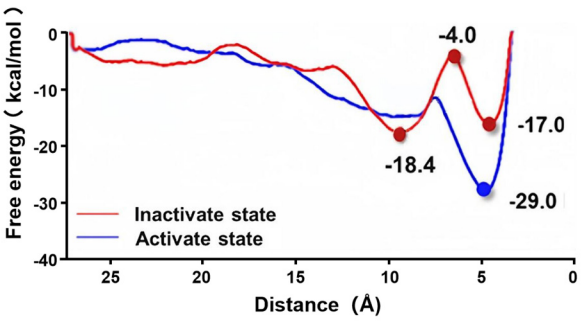

Figure 2. The free energy profile during the binding of the native substrate to Mpro in active and inactive state.

substrate and C145) with almost no energy barrier, and finally release 29.0 kcal/mol of energy to form a thermodynamically stable pre-reaction state, ensuring the subsequent occurrence of substrate hydrolysis. In the inactive state, although the substrate could also form a pre-reaction complex by releasing 17.0 kcal/mol of energy, the system first formed a thermodynamically more stable binding intermediate (with a distance of ~10 Å between the substrate and C145) before reaching the pre-reaction state. Thereafter, the system required overcoming an energy barrier of 14.4 kcal/mol to transition into the pre-reaction state. We speculate that due to the small volume of the catalytic pocket, when the substrate approaches the catalytic center to a distance of approximately 10 Å, it needs to induce the expansion of the pocket to achieve further binding. This conformational change results in the final pre-reaction state being thermodynamically and kinetically unstable, leading the substrate to tend to bind in a non-reactive manner (at a distance of ~10 Å from C145) and thus causing enzyme inactivation. These results indicate that an excessively small volume of the Mpro catalytic pocket hinders the effective binding between Mpro and its substrate, thereby rendering the enzyme inactive. Pelitinib appears to achieve inhibition of Mpro activity by inducing pocket contraction upon binding, as suggested by our simulations.

3.2. Conformational dynamics of the S3 helix modulate Mpro catalytic activity

Analysis of the MD trajectories of the Mpro structure revealed that the extended helical region spanning residues 40–60, herein defined as the "S3 helix," exhibited significantly higher flexibility in the active state, whereas its flexibility was markedly reduced in the inactive state (Figure 3A and B). This region encompasses the short P2 helix (residues 45–50) described previously (*47*), along with its extended flanking segments identified as key flexible regions in our simulations. The S3 helix is a component of the Mpro catalytic pocket, and H41 on the S3 helix forms a catalytic dyad with C145 located inside the pocket, which is the core of Mpro's hydrolytic function. Local structural analysis (Figure 3C and D) showed that in the active state, the hydrogen bond interaction between the H41-C145 dyad was disrupted, and the S3 helix was no longer constrained, thus moving away from the pocket. This may account for the high flexibility of the S3 helix and the enlarged volume of the Mpro catalytic pocket. In contrast, in the inactive state, the stable hydrogen bond interaction between H41 and C145 restricted the flexibility of the S3 helix and prevented its outward movement, ultimately leading to the shrinkage of the pocket volume. In other words, the interaction between H41 and C145 determines the flexibility of the S3 helix and ultimately affects the size of the Mpro catalytic pocket.

However, the enlarged volume of the Mpro catalytic pocket in the active state is dependent on the dissociation of the catalytic dyad (H41-C145), which contradicts the requirement for Mpro to exert subsequent hydrolytic activity (*i.e.*, a stable hydrogen bond interaction between the H41-C145 catalytic dyad). To resolve this contradiction, ABMD simulations were used to track the changes in the distance between H41 and C145, as well as the catalytic pocket volume, during the binding of the natural substrate (nsp4/5) to Mpro. As shown in Figure 4, with the entry of the substrate (evidenced by the reduced distance between the carbonyl carbon of P1-Gln and the sulfur atom of C145, labeled as d1), the distance between H41 and C145 (d2) decreased synchronously, and the catalytic pocket volume showed a significant contraction trend. When the substrate completed binding to Mpro (with d1 less than 5.0 Å), the pocket volume shrank to less than 1,000 $Å^3$, and d2 was stably maintained within 4 Å. These results indicate that the binding of the natural substrate can induce conformational rearrangement of the catalytic pocket, ultimately forming a stable H41-C145 catalytic dyad structure and a substrate-enzyme pre-reaction state, which is predicted to facilitate the subsequent hydrolysis.

3.3.The allosteric inhibition pathway of pelitinib in Mpro

From the protein structure displayed in Figure 5A and B, it is evident that the catalytic site and allosteric site of Mpro are spatially adjacent, and loop 141-145 directly connects these two regions. At the allosteric site, amino acids such as Y118, L141, and C300 exhibit obvious interactions with pelitinib. In this study, a series of Mpro variants were constructed by mutating these amino acids, and the changes in the catalytic pocket volume of each variant in the presence of pelitinib (Mpro-holo state) were calculated. As shown in Figure 5C, only four variants (L141A, S144A, C145A, and H41A) could reverse the pelitinib-induced contraction of the Mpro catalytic pocket volume, indicating that these

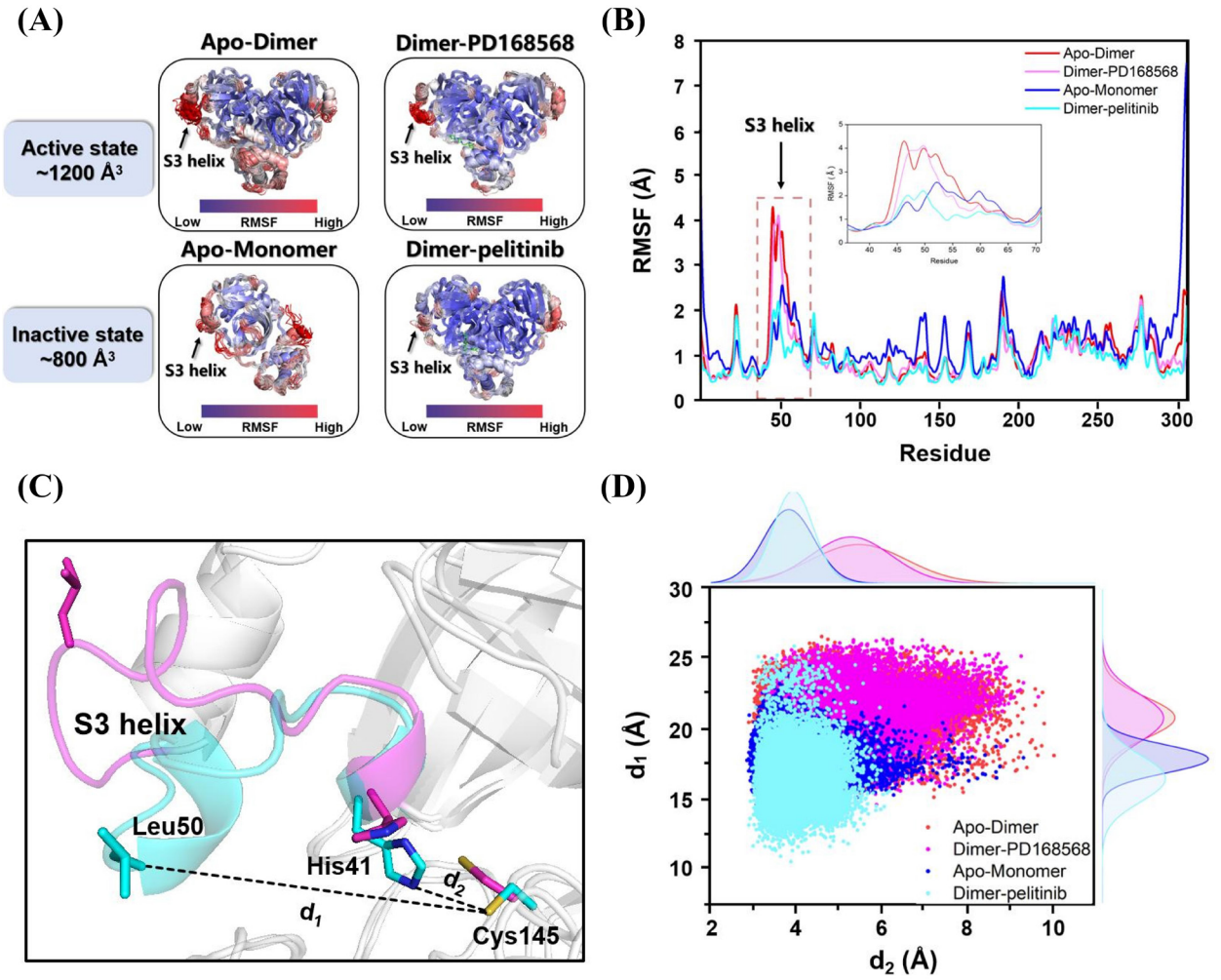

Figure 3. Conformational dynamics of Mpro in the active and inactive states. (A) Overall protein flexibility and **(B)** the Root Mean Square Fluctuation (RMSF) profile of Mpro. **(C)** Structural superposition of the S3 helix in the active and inactive states, and **(D)** statistical distribution of some key distances throughout the MD simulation trajectory.

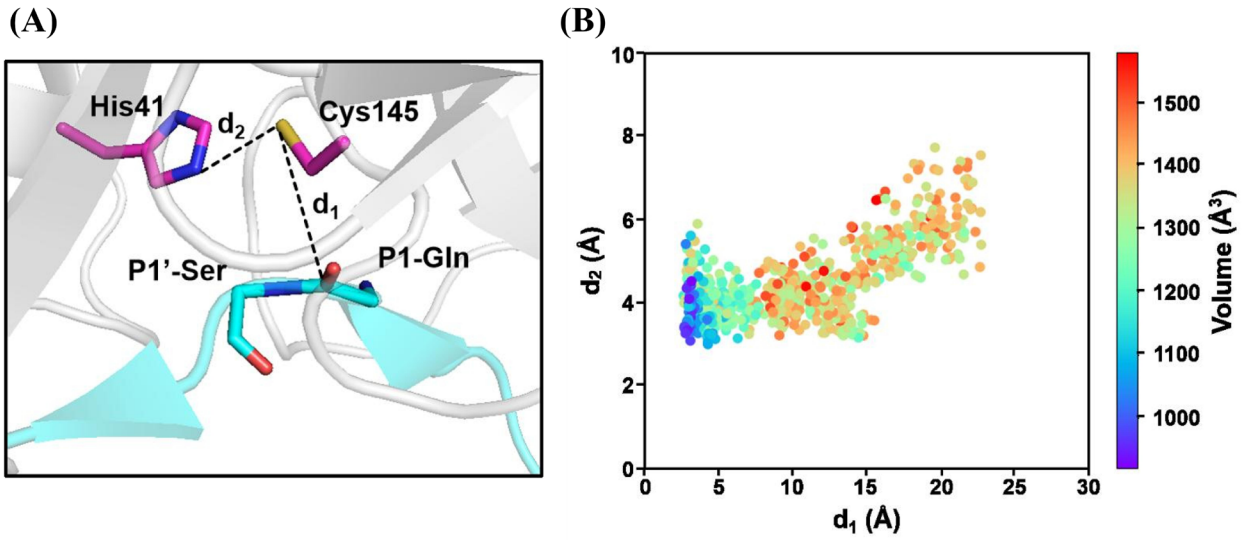

Figure 4. (A) Structure of the Mpro-native substrate (nsp4/5) complex. Key catalytic residues H41 and C145 (magenta), and the hydrolysis site in nsp4/5 (cyan), are shown in stick representation. Distances of C145-P1-Gln (d1) and H41-C145 (d2) are indicated by dashed lines. **(B)** Scatter plot of the distributions of d1 and d2. The color bar indicates the volume of Mpro catalytic pocket.

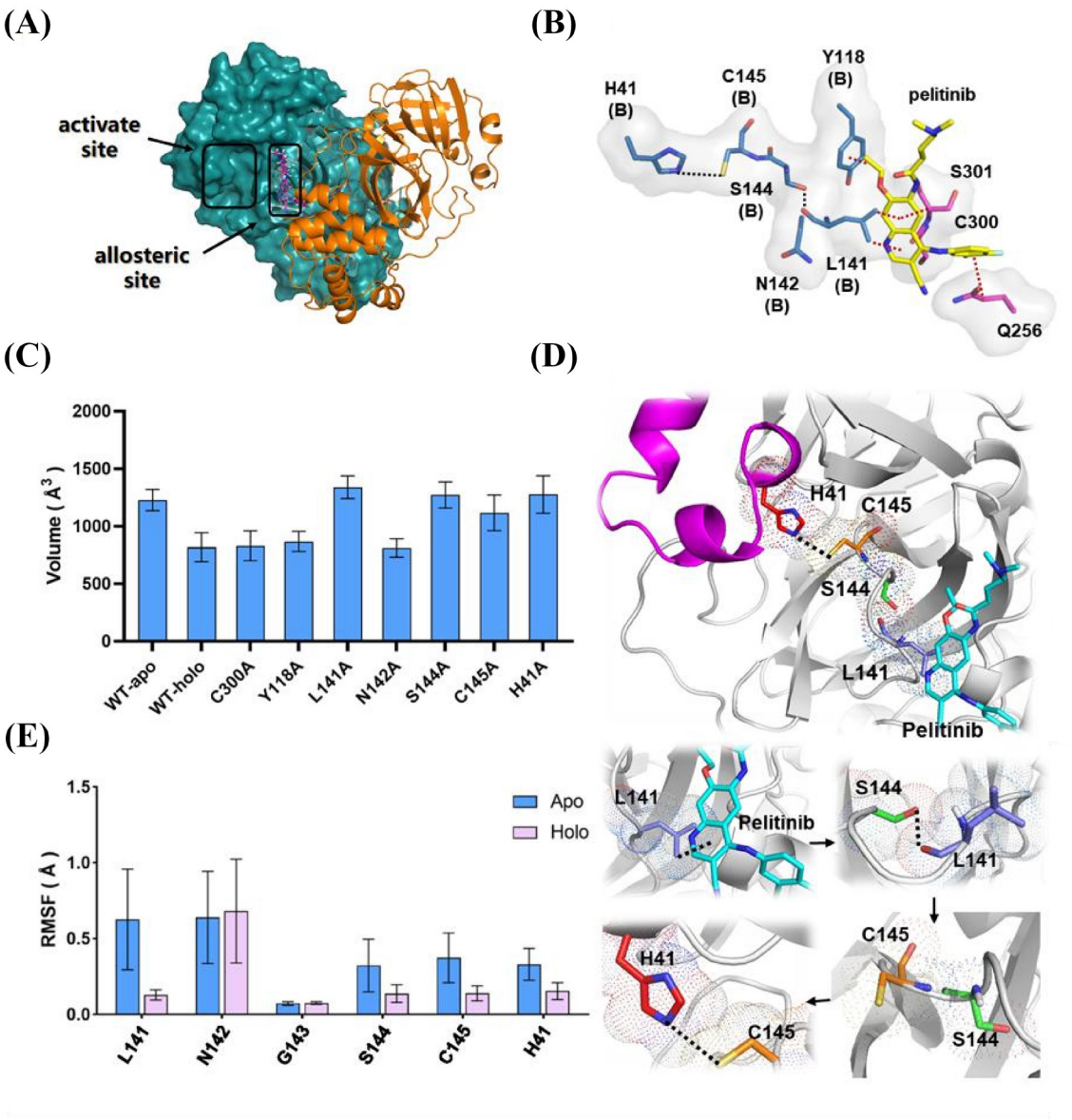

Figure 5. (A) Overall structure of the Mpro-Pelitinib complex. **(B)** Close-up view of the residues in active site and the allosteric site. **(C)** Catalytic pocket volumes of the Mpro wild-type and various mutants induced by pelitinib. **(D)** The allosteric regulatory pathway within the pelitinib-Mpro system. Pelitinib and key amino acid residues are shown in stick representation, and the S3 helix is depicted as a purple ribbon. **(E)** RMSF of key residues (L141, S144, C145, H41) along the allosteric pathway in both the Mpro Apo state and the Holo state (Pelitinib-Mpro system).

four amino acids play crucial roles in the allosteric inhibitory effect of Pelitinib. Additionally, the results of the C145A and H41A variants are consistent with our previous finding that the interaction between H41 and C145 affects the volume of the catalytic pocket.

Further analysis of the roles of these four key amino acids in the protein structure (Figure 5D) revealed that there was a CH-π interaction between the aromatic ring of the pelitinib backbone and the side chain of L141. Moreover, a hydrogen bond interaction existed between the main chain of L141 and the side chain of S144. Due to their adjacent positions in the amino acid sequence, the conformational changes of S144 are inevitably transmitted to C145. Based on these observations, we propose the following mechanism: Pelitinib restricts the flexibility of L141 through CH-π interaction, and this flexibility restriction effect is then transmitted to C145 *via* L141-S144. The reduced flexibility of C145 facilitates the maintenance of a stable hydrogen bond interaction between C145 and H41, which prevents the S3 helix from moving outward to expand the pocket. To verify this hypothesis, the root-mean-square fluctuation (RMSF) of loop 141-145 and H41 in both Mpro apo state and holo state (bound to pelitinib) was analyzed. As shown in Figure 5E, compared with the apo state, the flexibility of key amino acids in the pelitinib-mediated allosteric regulatory network (L141, S144, C145, and H41) was significantly reduced in the holo state. In contrast, no significant differences were observed in the flexibility of N142 and G143.

Collectively, these results are consistent with the view that pelitinib restricts the movement of the S3 helix through the L141-S144-C145-H41 interaction network, thereby maintaining the catalytic pocket in a small-volume state and ultimately blocking substrate binding to inhibit protein activity.

3.4. Compound screening and activity validation based on the allosteric mechanism

Given the potential off-target toxicity of pelitinib in anti-SARS-CoV-2 applications, this study further aimed to identify novel allosteric inhibitors of Mpro. The detailed screening workflow is shown in Figure S2 (*https://www.ddtjournal.com/action/getSupplementalData.php?ID=315*). By prioritizing the retention of the CH-π interaction with L141, a pharmacophore model based on the binding mode of pelitinib to the Mpro allosteric site was constructed. This model was then used for virtual screening against two subsets (Drug-like subset and Lead-like subset) of the ZINC20 database. Through a series of screening criteria, including molecular similarity evaluation and target affinity assessment, seven candidate compounds with higher affinity for Mpro than pelitinib were finally obtained (Figure S3, *https://www.ddtjournal.com/action/getSupplementalData.php?ID=315*). Subsequently, the pharmacokinetic properties and druggability (ADMET) of these seven compounds were predicted as listed in Table S2 (*https://www.ddtjournal.com/action/getSupplementalData.php?ID=315*). The results showed that Cpd-1 exhibited significant comprehensive advantages. Notably, Cpd-1 had no significant inhibitory effect on the cytochrome P450 enzyme system (CYP450), indicating a low risk of drug-drug interactions (DDI) and favorable metabolic safety profiles, which significantly enhance its potential as an Mpro inhibitor candidate.

Subsequently, a Cpd-1-Mpro complex model was successfully constructed *via* molecular docking. MD simulations combined with catalytic pocket volume analysis were performed to investigate the allosteric inhibitory activity of Cpd-1 against Mpro. The results showed that Cpd-1 could stably bind to the allosteric site of Mpro (Figure 6A and Figure S4, *https://www.ddtjournal.com/action/getSupplementalData.php?ID=315*), and importantly, it could form a stable CH-π interaction with L141, providing a structural basis for allosteric regulation. Further analysis of the

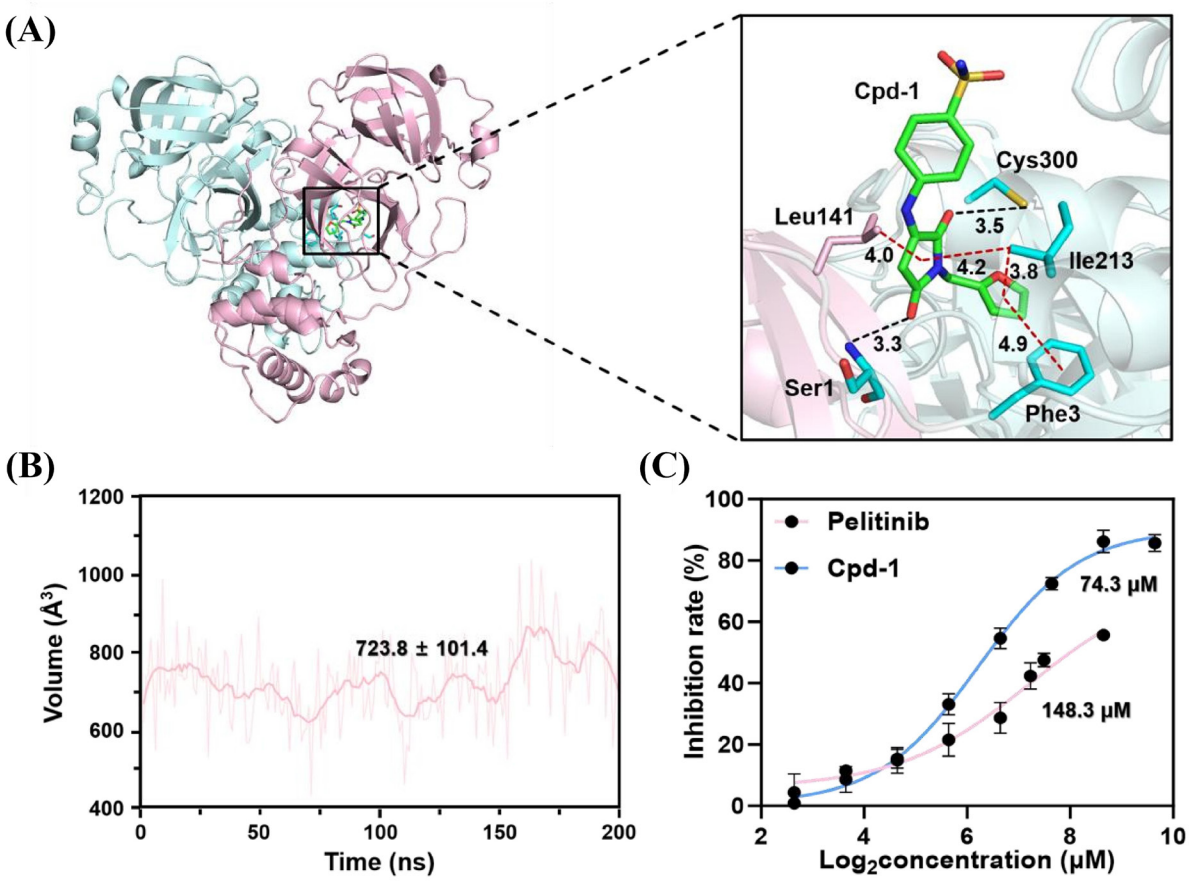

Figure 6. (A) The binding mode of Cpd-1 in Mpro. Cpd-1 (green), Leu141 (pink), and other key residues (cyan) are shown in stick representation. Hydrogen bond interactions (black) and CH-π interactions are indicated by dashed lines. Unit of the distance was used in Å. **(B)** Change in the catalytic pocket volume of Mpro in complex with Cpd-1 during the MD simulation. The average volume ± standard deviation is presented. **(C)** Inhibitory rate curve for Cpd-1 and pelitinib (as reference drugs) against SARS-CoV-2 Mpro by FRET assay (n = 3).

catalytic pocket volume of the Cpd-1-Mpro complex revealed that Cpd-1 also induced a reduction in the volume of the Mpro catalytic pocket (723.8 ± 101.4 Å^3 in Figure 6B), which was consistent with the behavior of the three previously identified positive compounds (pelitinib, RS102895, and ifenprodil, in Figure 1). This indicates that the newly identified compound (Cpd-1) also has potential allosteric inhibitory activity against SARS-CoV-2 Mpro. Subsequent fluorescence resonance energy transfer (FRET) assays (*48*) (Figure 6C) showed that Cpd-1 exhibited better Mpro inhibitory activity compared with pelitinib (74.3 μM *vs.* 148.3 μM), suggesting the potential of this newly identified compound as an Mpro inhibitor. However, we observed that the direct enzymatic IC_{50} of pelitinib determined in our cell-free FRET assay (148.3 μM) was substantially higher than its previously reported cellular antiviral EC_{50} (1.25 μM) (*27*). We hypothesize that this discrepancy arises because pelitinib is not a selective Mpro inhibitor, but rather a well-documented dual inhibitor of EGFR and Myt1 kinases. Previous studies have demonstrated that EGFR and related host kinase pathways participate in the entry and replication processes of SARS-CoV-2 (*49*). Accordingly, the potent cellular antiviral activity of pelitinib most likely stems from the synergistic effect of allosteric Mpro inhibition combined with the suppression of host kinase pathways essential for viral propagation. In our cell-free enzymatic system, the contribution of host targets is entirely eliminated, thus, the measured IC_{50} solely reflects the direct inhibitory potency of pelitinib against Mpro. Importantly, under strictly identical experimental conditions, Cpd-1 consistently exhibited stronger direct Mpro inhibitory activity than pelitinib, validating the success of our mechanism based screening strategy.

3.5. Target selectivity profile of Cpd-1

To investigate the target specificity of Cpd-1, the binding free energies of Cpd-1 and pelitinib to SARS-CoV-2 Mpro, Myt1 kinase, and EGFR were calculated based on MD simulations. Evaluation indicators such as RMSD, radius of gyration (Rg), solvent accessible surface area (SASA) and number of hydrogen bonds (Hbonds) showed that the MD simulations of all constructed ligand-protein systems reached a stable state (Figure S5, *https://www.ddtjournal.com/action/getSupplementalData.php?ID=315*), ensuring the reliability of the subsequent analysis results. As shown in Figure 7, the binding free energy of Cpd-1 to Mpro was -21.2 kcal/mol, which was comparable to that of pelitinib (-20.9 kcal/mol). However, the binding affinity of Cpd-1 to EGFR and Myt1 kinase was significantly weaker than that of pelitinib (-15.0 kcal/mol *vs.* -34.2

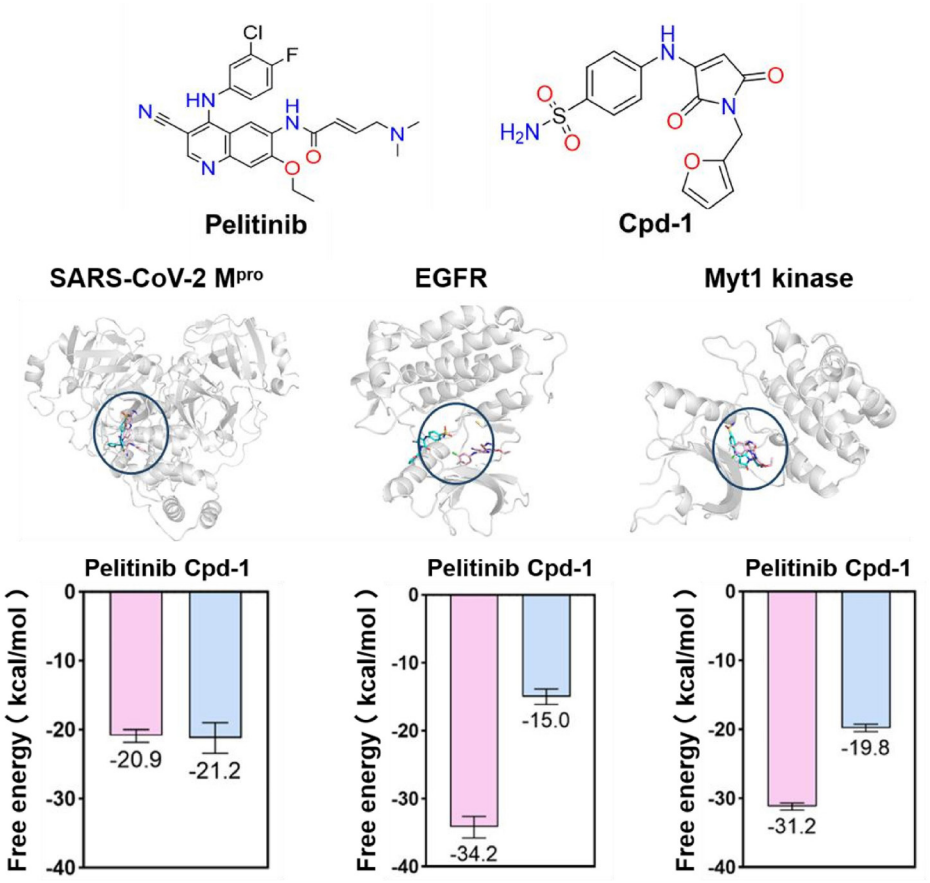

Figure 7. Structure, binding site, and binding free energy of Cpd-1 and pelitinib toward SARS-CoV-2 M^{pro}, EGFR, and Myt1 kinase.

kcal/mol for EGFR; -19.8 kcal/mol *vs.* -31.2 kcal/mol for Myt1 kinase). Additionally, Cpd-1 exhibited higher affinity for Mpro than for the other two targets. These results suggest that Cpd-1 not only retains Mpro inhibitory activity but also avoids non-specific binding to host EGFR and Myt1 kinase, thereby reducing potential side effects caused by off-target effects.

Subsequently, concentration-gradient experiments were conducted to evaluate the cytotoxicity of Cpd-1 and pelitinib. As shown in Figure 8, although both compounds exhibited concentration-dependent cytotoxic effects, their toxicity profiles differed significantly. Pelitinib induced significant cytotoxicity at a concentration of 10 μM, and almost completely inhibited cell growth at 50 μM. In contrast, Cpd-1 showed almost no cytotoxicity at 50 μM. Notably, even at a high concentration of 200 μM, the cell viability in the Cpd-1-treated group remained at approximately 60%, indicating that Cpd-1 has lower cytotoxicity and higher safety compared with pelitinib.

3.6. Computational predictions for selected mutant systems

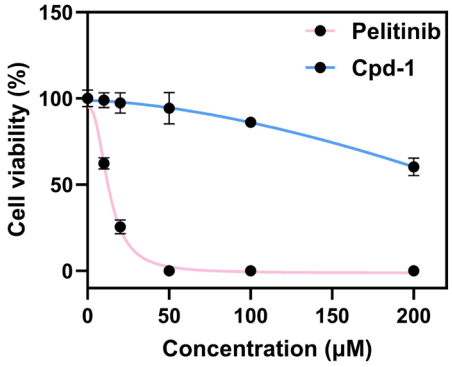

Figure 8. Cytotoxicity evaluation of Cpd-1 and pelitinib *in vitro* (*n* = 3).

Based on the findings that Cpd-1 exhibits higher Mpro inhibitory activity and lower cytotoxicity than pelitinib, this study further investigated the predicted inhibitory activity of Cpd-1 against drug-resistant mutants of SARS-CoV-2 Mpro through computational analysis. As shown in Figure 9, the catalytic pocket volume of a series of constructed Mpro drug-resistant mutants was approximately 1200 Å³ in the apo state, consistent with that of the wild-type Mpro. After binding to Cpd-1, the catalytic pocket volume of all mutants, including typical ensitrelvir-resistant strains (M49L and E166A) and nirmatrelvir-resistant strains (F140L, E166V and A193P), was reduced to approximately 800 Å³. These results demonstrate the potential inhibitory activity of Cpd-1 against various drug-resistant mutants of Mpro. These computational predictions suggest a potential strategy to overcome existing drug resistance barriers, warranting further experimental validation.

4. Discussion

In this study, we have systematically elucidated the allosteric inhibition mechanism of the SARS-CoV-2 main protease (Mpro) and successfully identified a novel inhibitor, Cpd-1, with the potential to overcome drug resistance. Unlike conventional active-site competitive inhibitors, allosteric modulation offers a distinct strategy to counter the rapid mutational evolution of Mpro. Our extensive MD simulations revealed that pelitinib binds to the allosteric site and, through the L141-S144-C145-H41 interaction network, restricts the flexibility of the S3 helix and stabilizes the H41-C145 catalytic dyad hydrogen bond. This series of conformational changes induces a marked contraction of the catalytic pocket from ~1,200 Å³ to ~800 Å³. This contraction thermodynamically and kinetically impedes the effective binding and hydrolysis of the natural substrate nsp4/5, providing, for the first time, an atomic-level depiction of how an allosteric inhibitor remotely modulates Mpro activity.

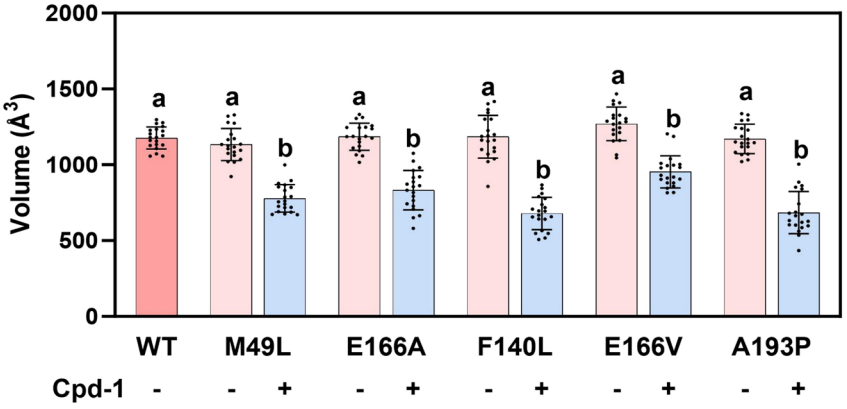

Figure 9. Catalytic pocket volumes of the SARS-CoV-2 Mpro wild-type, drug-resistant mutants, and the Cpd-1-bound drug-resistant mutants (a *vs.* b, $p < 0.0001$).

Guided by this mechanism, our structure-based virtual screening and subsequent biological validation led to the discovery of Cpd-1. This compound not only retains the critical CH-π interaction with L141 but also exhibits superior Mpro inhibitory activity (IC_{50} = 74.3 μM) compared to pelitinib (IC_{50} = 148.3 μM) in FRET-based enzymatic assays. More importantly, Cpd-1 demonstrates a significantly improved selectivity profile: computational binding free energy calculations show that its affinity for Mpro (-21.2 kcal/mol) is substantially higher than for the off-targets EGFR (-15.0 kcal/mol) and Myt1 kinase (-19.8 kcal/mol), whereas pelitinib shows strong nonspecific binding to both. These *in silico* findings are strongly corroborated by cytotoxicity assays, where Cpd-1 maintained ~ 60% cell viability even at a high concentration of 200 μM, while pelitinib nearly abolished cell growth at 50 μM. Collectively, these data robustly support a superior therapeutic window and safety profile for Cpd-1.

Notably, our computational predictions further indicate that Cpd-1 can effectively induce the same pocket contraction (from ~1,200 Å³ to ~800 Å³) in a panel of clinically relevant drug-resistant Mpro mutants, including E166V, F140L, and M49L. This suggests its potential for broad-spectrum anti-resistance activity. This characteristic is particularly significant for addressing future viral variants, as allosteric sites often exhibit higher sequence conservation than active sites, and the key residues we target, such as L141, are involved in a non-covalent conformational regulatory network that may be under lower mutational pressure.

Despite these promising findings, certain limitations should be acknowledged. The *in vitro* antiviral efficacy (EC_{50}) of Cpd-1, along with its *in vivo* pharmacokinetics and pharmacodynamics in animal models, remain to be validated. Furthermore, its inhibitory activity against resistant mutants is primarily based on computational models and requires confirmation through enzymatic and viral replication assays. Future efforts will focus on structure-based optimization of Cpd-1 to enhance its potency and drug-like properties, followed by comprehensive preclinical evaluation. Overall, our work not only deepens the mechanistic understanding of Mpro allosteric regulation but also provides a robust theoretical foundation and a promising candidate for the development of next-generation anti-coronavirus agents with a higher barrier to resistance.

5. Supporting Information

Summary of the MD simulation systems (Table S1, *https://www.ddtjournal.com/action/getSupplementalData.php?ID=315*), predicted pharmacokinetic properties and druggability (ADMET) of the screened compounds (Table S2, *https://www.ddtjournal.com/action/getSupplementalData.php?ID=315*). RMSD of Mpro monomer, Mpro dimer, and four ligand-Mpro complexes during the 500 ns MD simulation (Figure S1, *https://www.ddtjournal.com/action/getSupplementalData.php?ID=315*), screening workflow on the allosteric inhibitors of Mpro (Figure S2, *https://www.ddtjournal.com/action/getSupplementalData.php?ID=315*), structures and binding affinities of Pelitinib and the seven candidate compounds on Mpro (Figure S3, *https://www.ddtjournal.com/action/getSupplementalData.php?ID=315*), RMSD of Cpd-1-Mpro complex and distance changes of the key residues with Cpd-1 during the 200 ns MD simulation (Figure S4, *https://www.ddtjournal.com/action/getSupplementalData.php?ID=315*), evaluation indicators of MD simulation (RMSD, Rg, SASA and Hbonds) on the ligand-receptor complexes in Section 3.5 (Figure S5, *https://www.ddtjournal.com/action/getSupplementalData.php?ID=315*).

Funding: This work was supported by Natural Science Foundation of Shandong Province (ZR2024QH448), Key R&D Program of Shandong Province (2025CXPT137).

Conflict of Interest: The authors have no conflicts of interest to disclose.

Data availability statement: All data (input files for the MD simulations) are available on Github (*https://github.com/xwtangQDU/Allosteric-Inhibition-Mechanism-of-SARS-CoV-2-Main-Protease*).

References

1. Piret J, Boivin G. Pandemics throughout history. Front Microbiol. 2021; 11:631736.
2. Fauci AS. Infectious diseases: considerations for the 21st century. Clin Infect Dis. 2001; 32:675-685.
3. Nicola M, Alsafi Z, Sohrabi C, Kerwan A, Al-Jabir A, Iosifidis C, Agha M, Agha R. The socio-economic implications of the coronavirus pandemic (COVID-19): a review. Int J Surg. 2020; 78:185-193.
4. Karniadakis I, Mazonakis N, Tsioutis C, Papadakis M, Markaki I, Spernovasilis N. Oral Molnupiravir and Nirmatrelvir/Ritonavir for the treatment of COVID-19: a literature review with a focus on real-world evidence. Infect Dis Rep. 2023; 15:662-678.
5. Cao B, Wang Y, Lu H, *et al.* Oral simnotrelvir for adult patients with mild-to-moderate COVID-19. N Engl J Med. 2024; 390:230-241.
6. Chen X, Huang X, Ma Q, *et al*. Preclinical evaluation of the SARS-CoV-2 Mpro inhibitor RAY1216 shows improved pharmacokinetics compared with nirmatrelvir. Nat Microbiol. 2024; 9:1075-1088.
7. Syed YY. Ensitrelvir fumaric acid: first approval. Drugs. 2024; 84:721-728.
8. Kow CS, Hasan SS. Real-world effectiveness of BNT162b2 mRNA vaccine: a meta-analysis of large observational studies. Inflammopharmacology. 2021; 29:1075-1090.
9. Khobragade A, Bhate S, Ramaiah V, *et al.* Efficacy,

safety, and immunogenicity of the DNA SARS-CoV-2 vaccine (ZyCoV-D): the interim efficacy results of a phase 3, randomised, double-blind, placebo-controlled study in India. Lancet. 2022; 399:1313-1321.
10. Hadj Hassine I. COVID-19 vaccines and variants of concern: a review. Rev Med Virol. 2022; 32:e2313.
11. Graña C, Ghosn L, Evrenoglou T, *et al.* Efficacy and safety of COVID-19 vaccines. Cochrane Database Syst Rev. 2022; 12:CD015477.
12. McLean G, Kamil J, Lee B, Moore P, Schulz TF, Muik A, Sahin U, Türeci Ö, Pather S. The impact of evolving SARS-CoV-2 mutations and variants on COVID-19 vaccines. mBio. 2022; 13:e02979-21.
13. Madhi SA, Baillie V, Cutland CL, *et al.* Efficacy of the ChAdOx1 nCoV-19 Covid-19 vaccine against the B.1.351 variant. N Engl J Med. 2021; 384:1885-1898.
14. Hu Q, Xiong Y, Zhu G, Zhang Y, Zhang Y, Huang P, Ge G. The SARS-CoV-2 main protease (Mpro): structure, function, and emerging therapies for COVID-19. MedComm. 2022; 3:e151.
15. Bhardwaj M, Anjum R, Hariprasad P, Patel AK. Allosteric mutations impact the catalytic activity and oligomeric state of the main protease of coronavirus. Int J Biol Macromol. 2025; 309:142765.
16. Gioia M, Ciaccio C, Calligari P, De Simone G, Sbardella D, Tundo G, Fasciglione GF, Di Masi A, Di Pierro D, Bocedi A, Ascenzi P, Coletta M. Role of proteolytic enzymes in the COVID-19 infection and promising therapeutic approaches. Biochem Pharmacol. 2020; 182:114225.
17. Zhang L, Lin D, Sun X, Curth U, Drosten C, Sauerhering L, Becker S, Rox K, Hilgenfeld R. Crystal structure of SARS-CoV-2 main protease provides a basis for design of improved α-ketoamide inhibitors. Science. 2020; 368:409-412.
18. Liu Y, Liang C, Xin L, Ren X, Tian L, Ju X, Li H, Wang Y, Zhao Q, Liu H, Cao W, Xie X, Zhang D, Wang Y, Jian Y. The development of coronavirus 3C-like protease (3CLpro) inhibitors from 2010 to 2020. Eur J Med Chem. 2020; 206:112711.
19. Jin Z, Du X, Xu Y, *et al.* Structure of Mpro from SARS-CoV-2 and discovery of its inhibitors. Nature. 2020; 582:289-293.
20. Cannalire R, Cerchia C, Beccari AR, Di Leva FS, Summa V. Targeting SARS-CoV-2 proteases and polymerase for COVID-19 treatment: state of the art and future opportunities. J Med Chem. 2022; 65:2716-2746.
21. Lu H, Zhang G, Mao J, *et al*. Efficacy and safety of GST-HG171 in adult patients with mild to moderate COVID-19: a randomised, double-blind, placebo-controlled phase 2/3 trial. eClinicalMedicine. 2024; 71:102582.
22. Hattori SI, Bulut H, Hayashi H, *et al*. Structural and virologic mechanism of the emergence of resistance to Mpro inhibitors in SARS-CoV-2. Proc Natl Acad Sci U S A. 2024; 121:e2404175121.
23. Moghadasi SA, Biswas RG, Harki DA, Harris RS. Rapid resistance profiling of SARS-CoV-2 protease inhibitors. NPJ Antimicrob Resist. 2023; 1:9.
24. Wenthur CJ, Gentry PR, Mathews TP, Lindsley CW. Drugs for allosteric sites on receptors. Annu Rev Pharmacol. 2014; 54:165-184.
25. Cimermancic P, Weinkam P, Rettenmaier TJ, Bichmann L, Keedy DA, Woldeyes RA, Schneidman-Duhovny D, Demerdash ON, Mitchell JC, Wells JA, Fraser JS, Sali A. CryptoSite: expanding the druggable proteome by characterization and prediction of cryptic binding sites. J Mol Biol. 2016; 428:709-719.
26. Greener JG, Sternberg MJ. Structure-based prediction of protein allostery. Curr Opin Struct Biol. 2018; 50:1-8.
27. Günther S, Reinke PYA, Fernández-García Y, *et al.* X-ray screening identifies active site and allosteric inhibitors of SARS-CoV-2 main protease. Science. 2021; 372:642-646.
28. Samrat SK, Xu J, Xie X, Gianti E, Chen H, Zou J, Pattis JG, Elokely K, Lee H, Li Z, Klein ML, Shi PY, Zhou J, Li H. Allosteric inhibitors of the main protease of SARS-CoV-2. Antiviral Res. 2022; 205:105381.
29. Zhu JY, Cuellar RA, Berndt N, Lee HE, Olesen SH, Martin MP, Jensen JT, Georg GI, Schönbrunn E. Structural basis of Wee kinases functionality and inactivation by diverse small molecule inhibitors. J Med Chem. 2017; 60:7863-7875.
30. Hegedüs C, Truta-Feles K, Antalffy G, Várady G, Német K, Ozvegy-Laczka C, Kéri G, Orfi L, Szakács G, Settleman J, Váradi A, Sarkadi B. Interaction of the EGFR inhibitors gefitinib, vandetanib, pelitinib and neratinib with the ABCG2 multidrug transporter: implications for the emergence and reversal of cancer drug resistance. Biochem Pharmacol. 2012; 84:260-267.
31. Berman HM, Westbrook J, Feng Z, Gilliland G, Bhat TN, Weissig H, Shindyalov IN, Bourne PE. The Protein Data Bank. Nucleic Acids Res. 2000; 28:235-242.
32. Hollingsworth SA, Dror RO. Molecular dynamics simulation for all. Neuron. 2018; 99:1129-1143.
33. Case DA, Aktulga HM, Belfon K, *et al.* AmberTools. J Chem Inf Model. 2023; 63:6183-6191.
34. Tian C, Kasavajhala K, Belfon KAA, Raguette L, Huang H, Migues AN, Bickel J, Wang Y, Pincay J, Wu Q, Simmerling C. ff19SB: amino-acid-specific protein backbone parameters trained against quantum mechanics energy surfaces in solution. J Chem Theory Comput. 2020; 16:528-552.
35. Jorgensen WL, Chandrasekhar J, Madura JD, Impey RW, Klein ML. Comparison of simple potential functions for simulating liquid water. J Chem Phys. 1983; 79:926-935.
36. Bayly CI, Cieplak P, Cornell W, Kollman PA. A well-behaved electrostatic potential based method using charge restraints for deriving atomic charges: the RESP model. J Phys Chem. 1993; 97:10269-10280.
37. Ryckaert JP, Ciccotti G, Berendsen HJC. Numerical integration of the Cartesian equations of motion of a system with constraints: molecular dynamics of n-alkanes. J Comput Phys. 1977; 23:327-341.
38. Babin V, Roland C, Sagui C. Adaptively biased molecular dynamics for free energy calculations. J Chem Phys. 2008; 128:134101.
39. Wagner JR, Sørensen J, Hensley N, Wong C, Zhu C, Perison T, Amaro RE. POVME 3.0: software for mapping binding pocket flexibility. J Chem Theory Comput. 2017; 13:4584-4592.
40. Kumari R, Kumar R, Lynn A. G_mmpbsa – a GROMACS tool for high-throughput MM-PBSA calculations. J Chem Inf Model. 2014; 54:1951-1962.
41. Zoete V, Daina A, Bovigny C, Michielin O. SwissSimilarity: a web tool for low to ultra high throughput ligand-based virtual screening. J Chem Inf Model. 2016; 56:1399-1404.
42. Vilar S, Cozza G, Moro S. Medicinal chemistry and the Molecular Operating Environment (MOE): application

of QSAR and molecular docking to drug discovery. Curr Top Med Chem. 2008; 8:1555-1572.
43. Trott O, Olson AJ. AutoDock Vina: improving the speed and accuracy of docking with a new scoring function, efficient optimization, and multithreading. J Comput Chem. 2010; 31:455-461.
44. Daina A, Michielin O, Zoete V. SwissADME: a free web tool to evaluate pharmacokinetics, drug-likeness and medicinal chemistry friendliness of small molecules. Sci Rep. 2017; 7:42717.
45. Fu L, Shi S, Yi J, Wang N, He Y, Wu Z, Peng J, Deng Y, Wang W, Wu C, Lyu A, Zeng X, Zhao W, Hou T, Cao D. ADMETlab 3.0: an updated comprehensive online ADMET prediction platform enhanced with broader coverage, improved performance, API functionality and decision support. Nucleic Acids Res. 2024; 52:W422-W431.
46. Banerjee P, Kemmler E, Dunkel M, Preissner R. ProTox 3.0: a webserver for the prediction of toxicity of chemicals. Nucleic Acids Res. 2024; 52:W513-W520.
47. Kneller DW, Phillips G, O'Neill HM, Jedrzejczak R, Stols L, Langan P, Joachimiak A, Coates L, Kovalevsky A. Structural plasticity of SARS-CoV-2 3CL Mpro active site cavity revealed by room temperature X-ray crystallography. Nat Commun. 2020; 11:3202.
48. Zhao J, Ma Q, Zhang B, Guo P, Wang Z, Liu Y, Meng M, Liu A, Yang Z, Du G. Exploration of SARS-CoV-2 3CLpro inhibitors by virtual screening methods, FRET detection, and CPE assay. J Chem Inf Model. 2021; 61:5763-5773.
49. Razzaq A, Disoma C, Zhou Y, *et al*. Targeting epidermal growth factor receptor signalling pathway: a promising therapeutic option for COVID-19. Rev Med Virol. 2024; 34:e2500.

Received July 28, 2026; Revised August 18, 2026; Accepted August 22, 2026.

**Address correspondence to:*
Xiaowen Tang, School of Pharmacy, and Shandong Provincial Key Laboratory of Pathogenesis and Prevention of Brain Diseases, Qingdao University, Qingdao 266071, China.
E-mail: xwtang1219@qdu.edu.cn

Released online in J-STAGE as advance publication August 26, 2026.